Optics Communications 574 (2025) 131162

Contents lists available at ScienceDirect

Optics Communications

journal homepage: www.elsevier.com/locate/optcom

A U-shaped nanopillars metasurface with dual high Q for refractive index detection and polarization tunability

Jingwei Lv [a], Jianing Shi [a], Yanru Ren [a], Debao Wang [a], Weijie Kong [a], Qiang Liu [a], Wei Li [a], Ying Yu [a], Jianxin Wang [a], Wei Liu [a], Paul K. Chu [b,**], Chao Liu [a,*]

[a] School of Physics and Electronic Engineering, Northeast Petroleum University, Daqing, 163318, PR China
[b] Department of Physics, Department of Materials Science and Engineering, and Department of Biomedical Engineering, City University of Hong Kong, Tat Chee Avenue, Kowloon, Hong Kong Special Administrative Region of China

ARTICLE INFO

Keywords:
Metasurfaces
Fano shape
High Q-factors
Refractive index sensing
Optical switching

ABSTRACT

A metasurface composed of four U-shaped nanopillars of silicon and quartz as the substrate boasting excellent refractive index (RI) sensing and optical switching properties is designed and analyzed. By breaking the symmetry, the metasurface excites dual ultra-narrow quasi-bound states in the continuum (QBIC) resonance peaks with the Fano shape. Both peaks are located in the near-infrared region, and multipole analysis shows that the enhancement is caused by the toroidal dipole (TD) and electric quadrupole (EQ). Quality factors (Q-factors) of 41,898.34 and 20,563.17 and figure of merit (FOM) values of 2767 RIU^{-1} and 2314 RIU^{-1} are achieved, respectively. Additionally, the polarization characteristics of the metasurface are evaluated. The metasurface has excellent properties and practicality, and the results provide insights into the development of high-performance refractive index sensors and optical switches.

1. Introduction

The refractive index (RI), an inherent property of materials [1], is often used in material identification, quality control, chemical analysis, optical design, and environmental monitoring [2–6]. Metasurfaces are discrete subwavelength structures composed of artificial metaatoms [7]. Researchers have theoretically verified and prepared a wide range of metasurface devices, such as imaging polarimeters [8], image spectral processing [9], resonators [10] and sensors [11–13], based on the unique optical properties of metasurfaces. For instance, as RI sensors, metasurfaces utilize resonant properties to detect minute variations in the refractive index [14], thus offering enhanced precision in chemical analysis and environmental monitoring [15,16].

In these applications, the quality factors (Q-factors) and figure of merit (FOM) are critical parameters reflecting the efficiency of metasurfaces [17]. Metallic metasurfaces suffer from significant radiation losses due to the oscillation of free electrons [18], resulting in lower Q factors for resonant dips [19]. In contrast, all-dielectric metasurfaces exhibit sharper resonance peaks [20] with larger FOM and Q-factors [21]. Structures with bound states in the continuum (BIC) are natural high-Q resonators because the radiative Q is equal to infinity in the ideal case [22]. It has been shown that the conversion of BIC into QBIC and combination with Fano resonances typically produce large Q factors [23]. Recent reports have demonstrated the correlation between high Q-factor metasurfaces and BIC.

The BIC optical mode provides a destructive interference mechanism to accomplish high Q-factor resonance and strong field localization [24]. Ideally, BIC is a dark mode with infinite Q-radiation, which can neither be directly excited by incident light nor appear in the spectrum [25]. By breaking the symmetry of the unit cell, the primordial symmetric mode is broken, consequently allowing it to couple with the external continuum spectrum and transform into a QBIC with a finite Q-factor and non-zero linewidth [26,27]. In order to enhance QBIC mode excitation, some methods have been proposed, for example, breaking the symmetry of the all-dielectric metasurface by modifying certain parameters of the metasurface as well as changing the shape [28] and orientation [29] of the dielectric materials on the metasurface.

Song et al. [30] have proposed an all-dielectric hollow metasurface with a better Q-factor and revealed an inverse relationship between the radiative Q-factor and different asymmetries. However, the limited RI

* Corresponding author.
** Corresponding author.
E-mail addresses: paul.chu@cityu.edu.hk (P.K. Chu), msm-liu@126.com (C. Liu).

https://doi.org/10.1016/j.optcom.2024.131162
Received 4 August 2024; Received in revised form 22 September 2024; Accepted 26 September 2024
Available online 4 October 2024

sensitivity restricts detection in different environments in practice. Xing et al. [31] have designed a periodic structure by etching two semicircles and a connecting gap in the silicon nanocube, which shows Q-factor and FOM of 32,140 and 883 RIU^{-1}, respectively. Although this sensor has an improved Q-factor, there is no prominent increase in the FOM. Ma et al. [32] have reported an asymmetric all-dielectric metasurface with an FOM value of 2400 RIU^{-1} and shown that the multiple sharp Fano resonances have potential applications in refractive index sensors. However, despite recent advances, the design of a sensor with a high Q-factor and FOM capable of RI sensing is still challenging.

Herein, an all-dielectric metasurface with four U-shape nanopillars is designed to achieve high-sensitivity sensing based on QBICs in the near-infrared region. Structural perturbation is introduced to break the symmetry of the metasurface and convert the BIC into QBIC modes. By combining with symmetry-protected bound states in the continuum (SP-BIC), the QBICs fabricated by a series of multipole decompositions are verified by measuring the transmission spectra. The main electromagnetic sources of the two resonances are TD and EQ, respectively, leading to high Q-factors of 41,898.34 and 20,563.17 as well as FOM of 2767 RIU^{-1} and 2314 RIU^{-1}, respectively. The polarization dependence is studied for optical switching applications. Our results reveal the promising potential of photonic devices based on QBICs with high-Q factors in applications such as lasers, biosensors, and optical switching.

2. Metasurface design and theoretical analysis

2.1. Near-field properties

To support symmetry-protected BIC, a periodic asymmetric tetramer all-dielectric metasurface with in-plane symmetry is designed. Fig. 1(*a*) and (*b*) illustrate the conceptual 3-D views of metasurface. The period is $\boldsymbol{P} = 1000$ nm, the nanopillars are made of silicon (Si), and the substrate is quartz. The unit cell is displayed in the top view on the *xy*-plane in Fig. 1(*c*). The dimensions of the individual U-shape table are: semi-axis $\boldsymbol{r} = 100$ nm, table thickness $\boldsymbol{h1} = 450$ nm, and short rectangle length $\boldsymbol{w} = 140$ nm. The distances between the U-shape table pairs are $\boldsymbol{lx} = 560$ nm and $\boldsymbol{ly} = 500$ nm, respectively, and the substrate thickness is $\boldsymbol{H} = 1000$ nm. The refractive index of the Si and quartz substrate are set to n = 3.48 and n = 1.48 [33], respectively. Si and quartz used in this structure exhibit excellent optical properties in the near-infrared region. Utilize a plane wave as the structural light source, an X-polarized near infrared beam propagates perpendicularly along the negative z-axis, with its electric field vector oriented along the positive x-axis. The Floquet-periodic boundary conditions are applied in the x and y-directions, and the perfectly matched layer (PML) condition was applied above and under the unit cell [34] to absorb the radiation propagating to the boundary of the simulated area to avoid secondary effects on the simulation results. Depending on the element order in the model, a finer mesh is employed. The complete mesh consists of 28762 domain elements, 1286 boundary elements, and the PML contains 688 elements, The minimum element quality is equal to 0.0705. Wang et al. proposed a dual nanorods metasurface structure using semiconductor silicon [28]. The Si was deposited on a quartz substrate using magnetron sputtering, followed by baking to improve photoresist adhesion. Patterns were then created using electron-beam lithography (EBL), and the sample underwent development, etching, and washing to finalize the metasurface structure, which demonstrated high sensitivity and a high Q-factor. Similar silicon-based metasurface structures can be fabricated by the following steps: after cleaning the quartz substrate with ultrasonication [28], the silicon film can be deposited on it using low-pressure physical vapor deposition [35], followed by subsequent patterning of the silicon layer using standard EBL or reactive ion etching (RIE) [34].

To excite Fano resonances, the asymmetric parameter $\boldsymbol{N}$ is introduced. The scaling index of the graph in the upper left corner is defined as $\boldsymbol{N}$. Specifically, when $\boldsymbol{N} = 1$, the dimensions of the U-shape column in the upper left corner remain unchanged, resulting in congruent dimensions for all four nanopillars. $\boldsymbol{N} \neq 1$ means implies a change in the dimensions of the U-shape column in the upper left corner, while the dimensions of the others remain unchanged. The increase and decrease of $\boldsymbol{N}$ are defined as follows. When $\boldsymbol{N} < 1$, the size of the U-shape column decreases. Otherwise the size of the U-shape column increases. In order to visually illustrate the symmetry-breaking mechanism, the top view of the meta-unit is shown in Fig. 2(*a*). The optical response of the structure is simulated for different $\boldsymbol{N}$ to obtain the transmission spectra, as shown in Fig. 2(*b*).

By breaking the symmetry, this type of modification can be seamlessly combined with the BIC transformation in one unit. When $\boldsymbol{N} = 1$, the transmission spectrum from 1350 nm to 1475 nm is nearly flat, showing high transmittance. No transmission is visible. The transmission FWHM is close to 0, and the Q-factors approach infinity. While $\boldsymbol{N}$ changes, for example, $\boldsymbol{N} = 0.9$, two obvious transmissions appear at

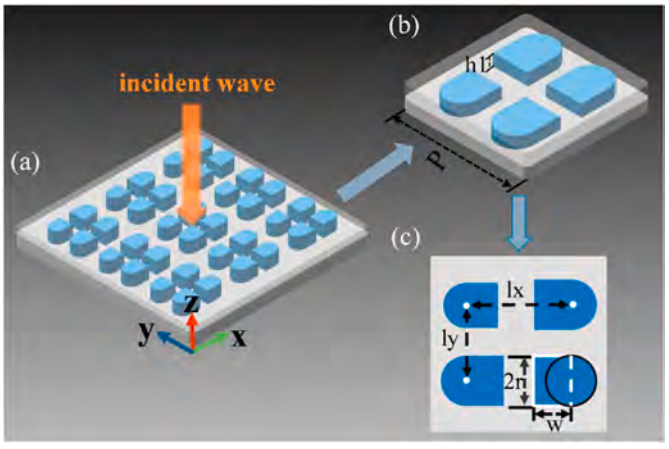

Fig. 1. (*a*) Schematic diagram of the asymmetric dimer metasurface, (*b*) Structure of a single unit cell, and (*c*) Top view of the metamaterial unit.

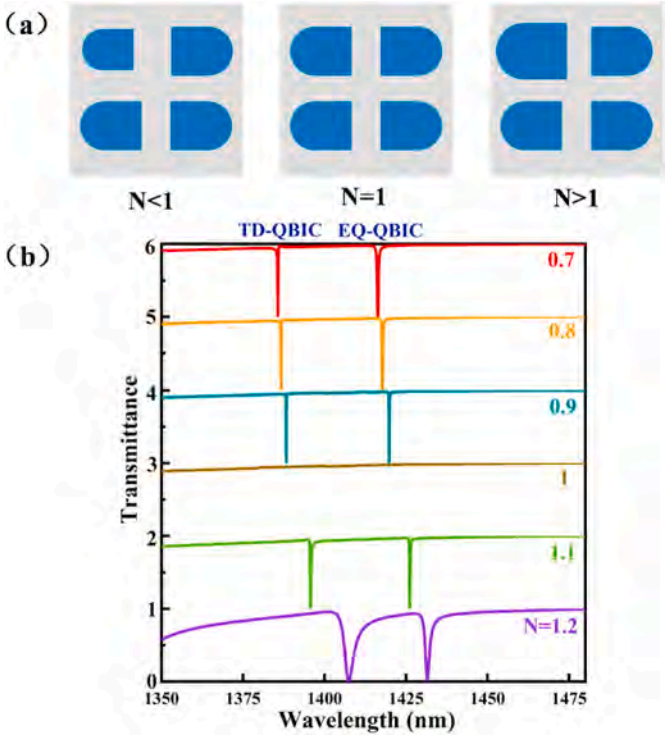

Fig. 2. (*a*) Destructive mechanics of the structural symmetry and (*b*) Transmission spectra of the metasurface showing the impact of different $\boldsymbol{N}$.

$\lambda 1 = 1388.27$ nm and $\lambda 2 = 1419.82$ nm, corresponding to TD-QBIC and EQ-QBIC resonances, respectively. The two Fano resonances are termed FR1 and FR2. It is noted that the center position of the nanopillar remains unchanged regardless of the variation in $\boldsymbol{N}$. In addition, the larger $\boldsymbol{N}$ deviates from 1, the wider the FWHM of the transmission and the lower the Q value.

To evaluate the physical mechanism of the generation of the two Fano resonances, the near-field of the metasurface can be decomposed into multipole expansion [34,36]. The electromagnetic field distribution indicates that a hybrid of multipoles contributes to the quasi-BIC. In order to quantify the contribution of multipoles to the resonance, we normally consider only the five strongest electromagnetic sources: electric dipole (ED), magnetic dipole (MD), toroidal dipole (TD), electric quadrupole (EQ), and magnetic quadrupole (MQ). The formulas for the pole moments are shown in the following [37,38]:

$$P = \frac{1}{i\omega}\int j d^3r \tag{1}$$

$$M = \frac{1}{2c}\int (r \times j) d^3r \tag{2}$$

$$T = \frac{1}{10c}\int \left[(r \times j)r - 2r^2 j\right] \tag{3}$$

$$Q_{\alpha\beta}^{(e)} = \frac{1}{2i\omega}\int \left[r_\alpha j_\beta + r_\beta j_\alpha - \frac{2}{3}(r \bullet j)\delta_{\alpha\beta}\right] d^3r \tag{4}$$

$$Q_{\alpha\beta}^{(m)} = \frac{1}{3c}\int \left[(r \times j)_\alpha r_\beta + (r \times j)_\beta r_\alpha\right] d^3r \tag{5}$$

where c is the vacuum light speed, and ω is the angular frequency. The combined subscripts of α and β can be x-y, y-z, and x-z, and separate α and β represent x–z, respectively.

The Q-factor is a crucial parameter affecting the resonator. The Fano resonance waveform is generally expressed by the following formula [39]:

$$T(\omega) = T_0 + G\frac{[q + 2(\omega - \omega_0)/\Gamma]^2}{1 + [2(\omega - \omega_0)/\Gamma]^2} \tag{6}$$

where $\omega_0 = 2\pi c/\lambda$ is the resonance angular frequency, c is the speed of light in vacuum, λ is the resonance wavelength, Γ is the resonance linewidth, T_0 is the background scattering parameter, G is the coupling coefficient between the continuous and discrete states, q is the Breit-Wigner-Fano parameter, which determines the asymmetry of the resonance curve, ω is the incident light angular frequency, and $T(\omega)$ is the transmittance [40]. In metasurface structures, the effective interaction of bright and dark modes can excite Fano resonance, and the difference in their resonance frequencies also influences the linearity of the Fano response [41,42].

Fig. 3(*a*) shows the simulated curve aligns well with the fitted curve. Fig. 3(*b*) presents the multipolar contributions (up to the quadrupole) of FR1. As shown in the electric field diagram in Fig. 3(c), two sets of current loops are established within the nanowires. In the cross-section of the left nanopillar, the field arrows (head-to-tail) rotate clockwise along the z-direction, whereas, in the right nanopillar, the field arrows rotate in the opposite direction. It can be observed that the displacement currents in the ellipsoidal nanopillars twist in opposite directions, generating four longitudinal magnetic moments oriented along the y-axis, as indicated by the white arrows in Fig. 3(d). This not only confirms the presence of MQ [43], but also reveals that the direction arrows of the magnetic fields form a loop and circulate clockwise in the y-direction,

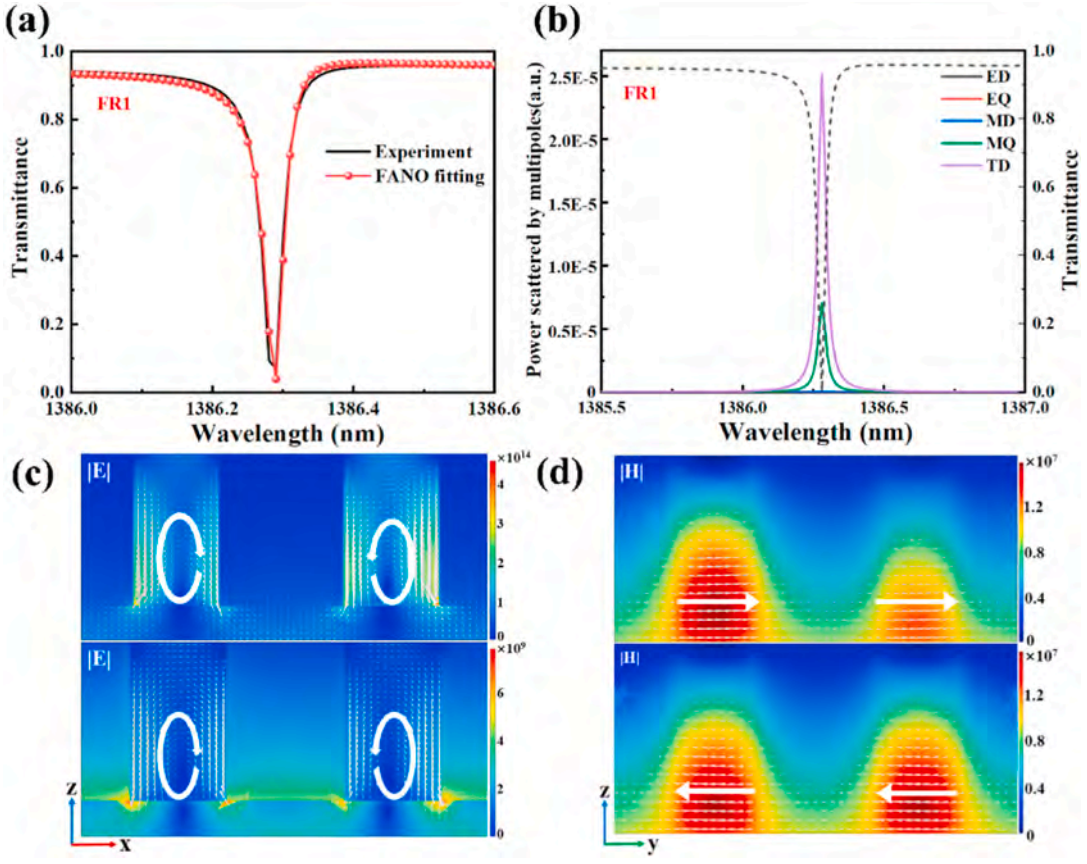

Fig. 3. (*a*) Results of FR1 with the black line representing the simulated results and the red line showing the fitted results; (*b*) Multipolar decomposition of FR1; (*c*) Electric field distributions of FR1 in the *xz*-plane; (*d*) Magnetic field distributions of FR1 in the *yz*-plane.

which characterizes TD [44]. Previous researchers have found that the TD resonance can be effectively excited by constructing elementary surface structure of tetramer clusters [45] and our structural model also confirms this conclusion.

Fig. 4(*a*) presents the Fano fitting result for FR2 when $\boldsymbol{N} = 0.9$, and Fig. 4(*b*) shows that the contribution of EQ dominates FR2 resonance. Obviously, the EQ contribution dominates the response, followed by MD and MQ. The electric field distributions of FR2 in the *xz*-plane are shown in Fig. 4(*c*). The electric field is distributed around the external side and between the gaps in the tetramer. The existence of EQ in the *xy*-plane is proven by the vortex of the displacement current [white arrows in Fig. 4 (*c*)]. Fig. 4(*d*) shows the corresponding magnetic field distributions in the *xy*-plane. The magnetic field is mainly located inside the structure, and the magnetic vectors distinctly exhibit the salient features of MD.

2.2. Influence of size

To analyze the dependence of resonance on the geometric parameters of the unit, the changes in the transmission curves of the metasurface are derived for different substrate thicknesses (***H***), substrate thicknesses (***h1***), substrate dimensions (***P***), and rectangular widths (***w***). The initial parameters are: $\boldsymbol{P} = 1000$ nm, $\boldsymbol{h1} = 450$ nm, $\boldsymbol{lx} = 280$ nm, $\boldsymbol{r} = 100$ nm, $\boldsymbol{ly} = 250$ nm, $\boldsymbol{w} = 140$ nm, $\boldsymbol{H} = 1000$ nm, and $\boldsymbol{N} = 0.9$.

The dependence of transmission spectra on changes in the substrate dimensions (***P***) is assessed while other parameters are fixed. As shown in Fig. 5, the resonance of FR1 and FR2 exhibits a significant redshift with increasing P in 10 nm increments, which is attributed to the reduction of the effective dielectric permittivity of the resonance response due to the geometric scale effect [46]. Fig. 5 shows that the changes in ***P*** have a negligible impact on the transmissivity. However, they affect the resonant frequency, and adjusting ***P*** modulates the resonance frequency.

The impact of ***H*** on the transmission spectra is evaluated. The wavelength range is between 1360 nm and 1460 nm, and the substrate thickness is changed from 940 nm to 1060 nm, while the Fano resonance profiles FR1 and FR2 redshift. Meanwhile, the transmittance is not linearly related to the H, as shown in Fig. 6(*a*). Firstly, the transmittance increases as ***H*** increases when ***H*** is less than 1000 nm. However, when ***H*** exceeds 1000 nm, the transmittance decreases as ***H*** increases. The change in transmittance in Fig. 6(*a*) is not significant. Therefore, a compromise of $\boldsymbol{H} = 1000$ nm is selected. Fig. 6(*b*) displays the simulated transmission spectra for different substrate thicknesses (***h1***). As the

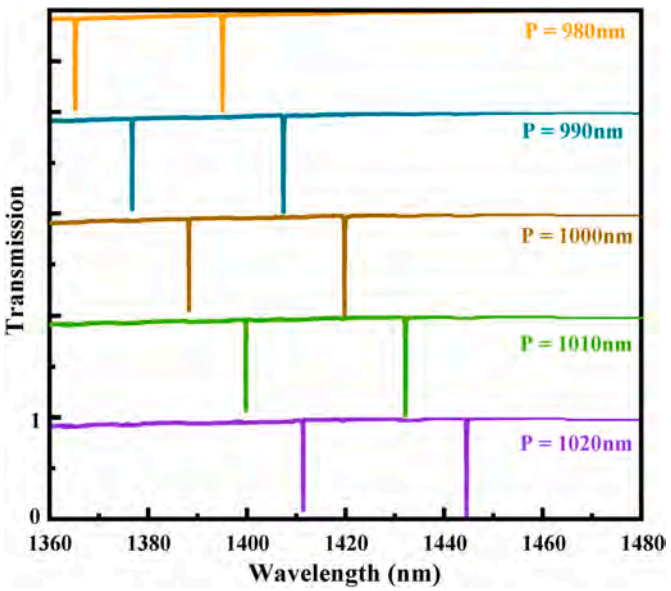

Fig. 5. Transmission spectra of silicon nanorods with different substrate dimensions (***P***).

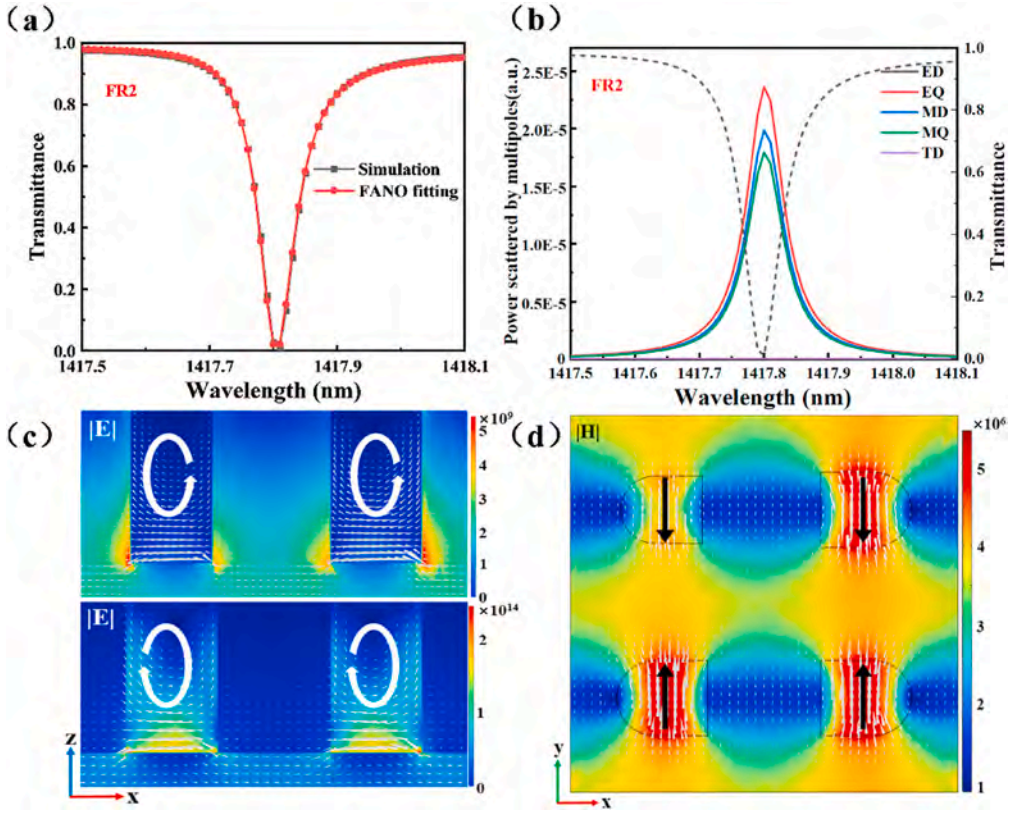

Fig. 4. (*a*) Transmission spectra and fitted results based on the Fano formula for FR2; (*b*) Multipolar decomposition of FR2; (*c*) Electric field distributions of FR2 in the *xz*-plane; (*d*) Magnetic field distributions of FR2 in the *xy*-plane.

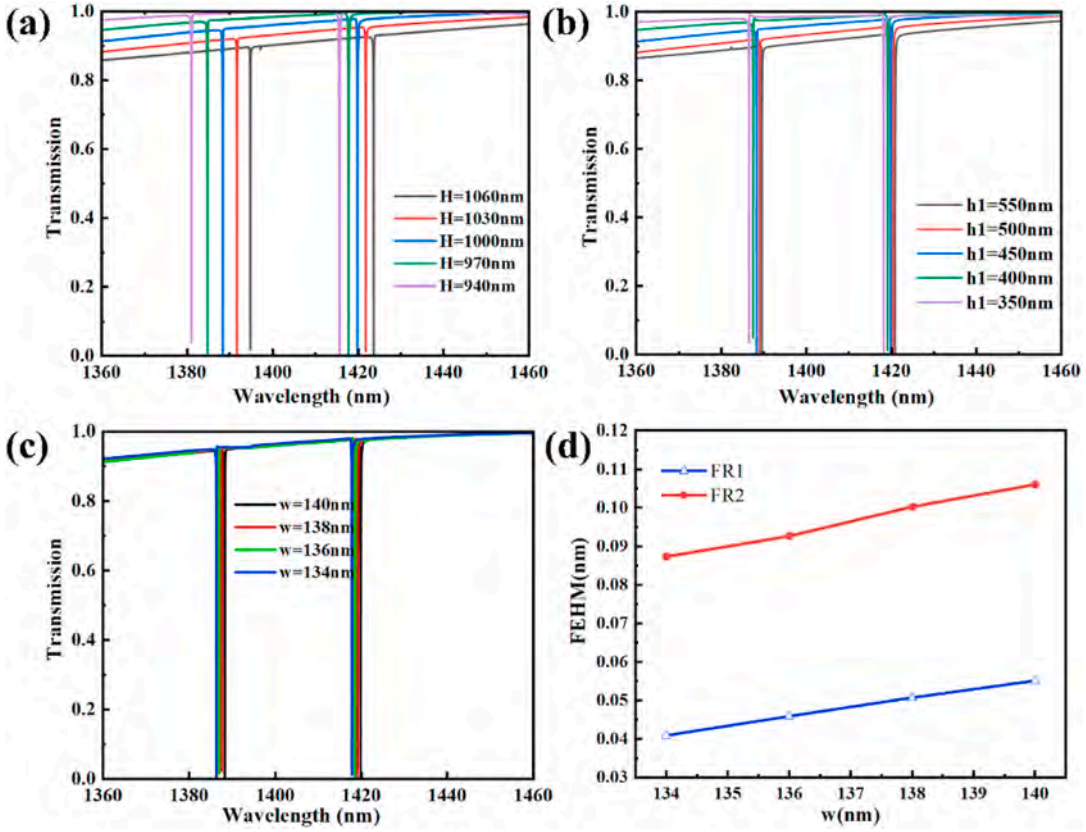

Fig. 6. (*a*) Transmission spectra of silicon nanorods with different substrate thickness (***H***), (*b*) Height of silicon nanorods ***h1***, and (*c*) Rectangular width ***w***; (*d*) Dependence of line width on rectangle width ***w***.

length h1 of the silicon nanorods increases from 350 nm to 550 nm, the resonant wavelengths of the transmission peaks FR1 and FR2 redshift, and the shift decreases successively. The reason for the redshift is that increasing the length of ***h1*** increases the medium oscillator volume V (x, y, z) [47]. Adjusting ***H*** and ***h1*** can also regulate the position of the resonance wavelength and improve the modulation depth.

Fig. 6(c) displays the simulated transmission spectra for different rectangular widths (w), which increase uniformly from 134 nm to 140 nm. The resonant wavelengths of FR1 and FR2 blueshift slightly with decreasing rectangular width. Fig. 6(*d*) shows that the linewidth of the transmission dip is directly proportional to the width of the rectangle. As a result, $\boldsymbol{w} = 134$ nm is chosen.

3. Applications

3.1. Sensors based on the QBIC

In RI sensing, a high Q-factor and strong field enhancement are important, and hence, a high Q-factor of resonance FR1 and FR2 is necessary. Here, common liquids used in biomedical and sensing

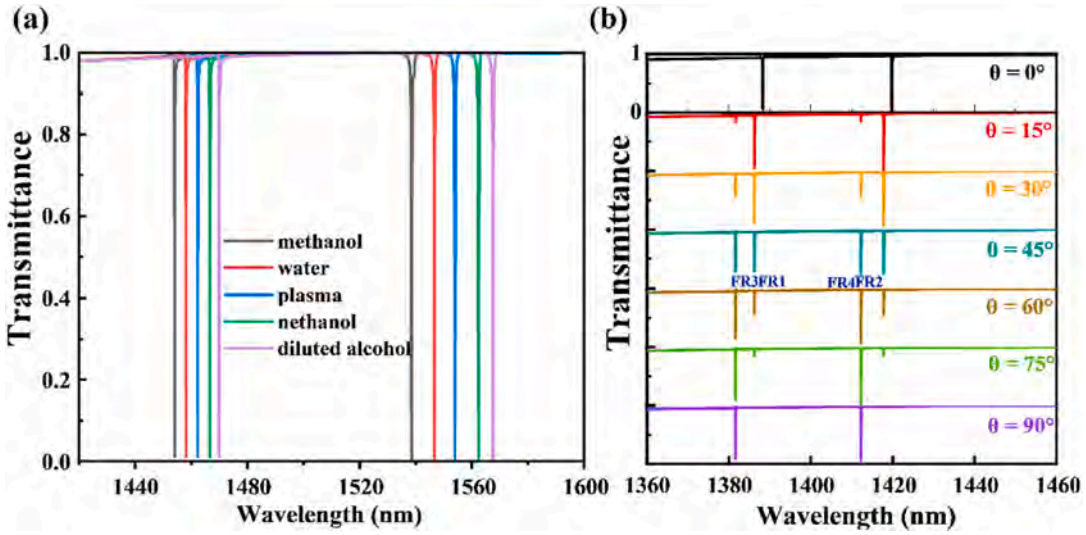

Fig. 7. Transmittance spectra of the mode I versus refractive index for (*a*) Different biological environments and (*b*) Different polarization angles (***θ***).

applications are chosen to assess the transmission of the metamaterial for different refractive indexes. The refractive index range between 1.319 and 1.36 is selected based on the following: methanol ($n_{methanol}$ = 1.319), water (n_{water} = 1.33), plasma (n_{plasma} = 1.341), ethanol ($n_{ethanol}$ = 1.352), and diluted alcohol ($n_{diluted\ alcohol}$ = 1.36). The unified nomenclature "n_p" is used for the refractive index. Fig. 7(*a*) shows the transmission spectra of resonances FR1 and FR2 with the gap and surroundings filled with different liquids. When N = 0.9, the Q-factors for FR1 and FR2 are 41,898.34 and 20,563.17, respectively.

The sensing properties of the all-dielectric metasurface are studied. The Q-factor in the near-infrared region is defined as follows:

$$Q = \frac{f_0}{X_{FWHM}} \tag{7}$$

where f_0 is the resonance frequency, and XFWHM is the FWHM of the transmission spectrum. The sensor sensitivity (S) is defined as follows.

$$S = \frac{\Delta\lambda}{\Delta n} \tag{8}$$

$$FOM = \frac{S}{X_{FWHM}} \tag{9}$$

where $\Delta\lambda$ is the wavelength shift caused by the refractive index change Δn, and FWHM is the full-width at half-maximum of the resonance.

Fig. 7(*a*) shows that when significant redshifts occur in FR1 and FR2 and taking $n_{methanol}$ = 1.319 compared to n_0 = 1.0 as an example, the redshift ranges for FR1 and FR2 are 67.82 nm and 120.75 nm, respectively. When the proposed metasurface is applied to refractive index sensing, the sensitivity reaches up to 386.83/707.31 GHz/RIU, with a corresponding FOM of 2767.37/2314.23 RIU−1. The refractive index linearity calculations for the FR1 are R^2_{FR1} = 0.96993 [48].

3.2. Optical switching based on QBIC

To further study the influence of the symmetry on FR1 and FR2, the transmission spectra for varying polarization angles θ ranging from 0° to 90° are derived and displayed in Fig. 7(*b*). The transmission spectra change with the polarization angles, indicating polarization correlation. As θ increases from 0° to 90°, the transmission amplitudes of resonances FR1 and FR2 decrease, while those of FR3 and FR4 increase. Similar to most symmetrical QBIC resonances, FR1 and FR2 are polarization-selective. By rotating the polarization direction, the incident beam is progressively changed from x polarized (θ = 0°) to y polarized (θ = 90°), and the magnitude of FR1andFR2 gradually decreases until the resonance disappears in the transmission spectrum, while new resonances FR3 and FR4 appear. With regard to polarization dependence, the resonance shows a bidirectional change from (0, 1, 0, 1) to (1, 0, 1, 0), when θ changes from 0° to 90°. It suggests that the metasurface has potential in bidirectional optical switching. In Table 1, by comparing the reported sensors in terms of Q factor, sensitivity, structural design, and materials, it is demonstrated that the proposed all-dielectric metasurface sensing structure exhibits a high Q factor, high sensitivity, and high FOM characteristics, with theoretical comprehensive performance parameters surpassing those of similar dielectric metasurface sensors.

4. Conclusion

A metasurface consisting of four silicon cylinders intersecting rectangular blocks and a quartz substrate is designed and analyzed. Two sharp Fano resonances corresponding to TD-QBIC and EQ-QBIC in the transmission spectra of the in-plane symmetry-broken metasurface in the near-infrared region are observed. The resonant frequency and linewidth can be altered by modifying the asymmetric parameters of the nanorods. When the asymmetric parameter N is 0.9, the Q-factors are 41,898.34 and 20,563.17, and the FOM values are 2767 RIU^{-1} and 2314 RIU^{-1}, respectively. The feasibility of refractive index sensing and polarization angle sensing are investigated. The metasurface is demonstrated to be an excellent refractive index sensor with high sensitivity and bidirectional optical switching by controlling the polarization direction of the incident light. The metasurface thus has promising prospects in biosensing and optical switching.

Table 1
Comparison of different BIC-based metasurface sensors.

structure	RI sensitivity	FOM (Max)	Q-factor (Max)	References
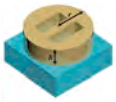	160 nm/RIU, 115 nm/RIU	575RIU^{-1}	17,106	[30]
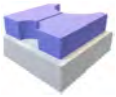	265 nm/RIU, 265 nm/RIU	883 RIU^{-1}	32,140	[31]
	240 nm/RIU, 260 nm/RIU, 135 nm/RIU	675 RIU^{-1}	47,000	[49]
	402 nm/RIU	2400 RIU^{-1}	8422	[32]
	386 nm/RIU, 707nm/RIU	2767 RIU^{-1},	41,898	This work

CRediT authorship contribution statement

Jingwei Lv: Methodology. **Jianing Shi:** Writing – original draft. **Yanru Ren:** Supervision. **Debao Wang:** Formal analysis. **Weijie Kong:** Data curation. **Qiang Liu:** Software. **Wei Li:** Supervision. **Ying Yu:** Software. **Jianxin Wang:** Supervision. **Wei Liu:** Investigation. **Paul K. Chu:** Validation. **Chao Liu:** Project administration.

Declaration of competing interest

The authors declare no conflicts of interest.

Data availability

Data will be made available on request.

Acknowledgments

This work was jointly supported by the National Natural Science Foundation of China [12304480], Heilongjiang Provincial Natural Science Foundation of China [JQ2023F001], Local Universities Reformation and Development Personnel Training Supporting Project from Central Authorities, Natural Science Foundation of Heilongjiang Province [LH2021F007], China Postdoctoral Science Foundation funded project [2020M670881], Study Abroad returnees merit based Aid Foundation in Heilongjiang Province [070–719900103], City University of Hong Kong Strategic Research Grant (SRG) [7005505], as well as City University of Hong Kong Donation Research Grants [DON-RMG 9229021 and 9220061].

References

[1] J. Kim, H. Kim, B. Kim, et al., Highly tunable refractive index visible-light metasurface from block copolymer self-assembly, Nat. Commun. 7 (2016) 12911.
[2] D. Ray, T.V. Raziman, C. Santschi, et al., Hybrid metal-dielectric metasurfaces for refractive index sensing, Nano Lett. 20 (2020) 8752–8759.
[3] Y. Cheng, Z. Li, Z. Cheng, Terahertz perfect absorber based on InSb metasurface for both temperature and refractive index sensing, Opt. Mater. 117 (2021) 111129.
[4] Z. Jakšić, S. Vuković, J. Matovic, D. Tanasković, Negative refractive index metasurfaces for enhanced biosensing, Materials 4 (2011) 1–36.
[5] G. Liu, X. Zhai, L. Wang, et al., A high-performance refractive index sensor based on Fano resonance in Si split-ring metasurface, Plasmonics 13 (2018) 15–19.
[6] J. Hu, T. Lang, G. Shi, Simultaneous measurement of refractive index and temperature based on all-dielectric metasurface, Opt Express 25 (2017) 15241–15251.
[7] Z. Wang, Y. Zheng, M. Ouyang, H. Fan, Q. Dai, H. Liu, L. Wu, High-Q quasi-bound states in the continuum in C2-symmetric metasurface with enhanced second harmonic generation in two-dimensional materials, Opt Laser. Technol. 176 (2024) 110868.
[8] Z. Huang, Y. Zheng, J. Li, et al., High-resolution metalens imaging polarimetry, Nano Lett. 23 (23) (2023) 10991–10997.
[9] M. Deng, M. Cotrufo, J. Wang, et al., Broadband angular spectrum differentiation using dielectric metasurfaces, Nat. Commun. 15 (1) (2024) 2237.
[10] B. Cai, L. Yang, L. Wu, et al., Dual-narrowband terahertz metamaterial absorber based on all-metal vertical ring array for enhanced sensing application, Phys. Scripta 99 (9) (2024) 095503.
[11] Y. He, B. Cai, L. Wu, et al., Tunable VO2 metasurface for reflective terahertz linear and circular polarization wavefront manipulation at two frequencies independently, Phys. B Condens. Matter 681 (2024) 415848.
[12] B. Cai, L. Wu, X. Zhu, et al., Ultra-broadband and wide-angle plasmonic light absorber based on all-dielectric gallium arsenide (GaAs) metasurface in visible and near-infrared region, Results Phys. 58 (2024) 107509.
[13] B. Cai, X. Zhu, L. Wu, L. Yang, Y. Cheng, Visible quintuple narrowband metasurface absorber based on gallium arsenide square cavity for multispectral sensing application, IEEE Sensor. J. 24 (12) (2024) 19229–19236.
[14] Y. Zhong, L. Du, Q. Liu, L. Zhu, B. Zhang, Metasurface-enhanced ATR sensor for aqueous solution in the terahertz range, Opt Commun. 465 (2020) 125508.
[15] A. Vestri, M. Rippa, V. Marchesano, D. Sagnelli, G. Margheri, J. Zhou, L. Petti, LSPR immuno-sensing based on iso-Y nanopillars for highly sensitive and specific imidacloprid detection, J. Mater. Chem. B 9 (2021) 9153–9161.
[16] F. Yesilkoy, E. Arvelo, Y. Jahani, et al., Ultrasensitive hyperspectral imaging and biodetection enabled by dielectric metasurfaces, Nat. Photonics 13 (2019) 390–396.
[17] B. Meng, J. Wang, C. Zhou, et al., Bound states in the continuum supported by silicon oligomer metasurfaces, Opt Lett. 47 (2022) 1549–1552.
[18] X. Zhao, C. Chen, K. Kaj, I. Hammock, Y. Huang, R.D. Averitt, X. Zhang, Terahertz investigation of bound states in the continuum of metallic metasurfaces, Optica 7 (2020) 1548–1554.
[19] P. Lalanne, P. Chavel, Metalenses at visible wavelengths: past, present, perspectives, Laser Photon. Rev. 11 (2017) 1600295.
[20] K. Deng, Y. Gao, Y. Gao, X. Fan, T. Wu, Tunable high-Q metasurface for terahertz optical switching and sensing, Optik 288 (2023) 171172.
[21] J. Li, L. Ye, Dielectric dual-dimer metasurface for enhanced mid-infrared chiral sensing under both excitation modes, Nanophotonics 12 (2023) 2189–2197.
[22] C. Hsu, B. Zhen, A.D. Stone, et al., Bound states in the continuum, Nat. Rev. Mater. 1 (2016) 1–13.
[23] C. Liu, W. Liu, W. Li, et al., Design of simple, ultrasensitive, and tunable teraherz metasensors based on quasi-BIC, Opt Commun. 550 (2024) 129967.
[24] L. Huang, R. Jin, C. Zhou, G. Li, L. Xu, Ultrahigh-Q guided mode resonances in an All-dielectric metasurface, Nat. Commun. 14 (2023) 3433.
[25] N. Liu, S. Wang, J. Lv, J. Zhang, Achiral nanoparticle trapping and chiral nanoparticle separating with quasi-BIC metasurface, Opt Express 31 (2023) 28912–28928.
[26] E.N. Bulgakov, A.F. Sadreev, Bound states in the continuum in photonic waveguides inspired by defects, Phys. Rev. B Condens. Matter 78 (2008) 075105.
[27] D. Marinica, A. Borisov, S. Shabanov, Bound states in the continuum in photonics, Phys. Rev. Lett. 100 (2008) 183902.
[28] T. Wang, S. Liu, J. Zhang, L. Xu, M. Yang, D. Ma, Dual high-Q Fano resonances metasurfaces excited by asymmetric dielectric rods for refractive index sensing, Nanophotonics 13 (2024) 463–475.
[29] J. Feng, X. Wang, J. Cheng, M. Zeng, Polarization-independent bound state in the continuum without the help of rotational symmetry, Optics Letter 48 (2023) 4829–4832.
[30] S. Song, S. Yu, H. Li, T. Zhao, Ultra-high Q-factor toroidal dipole resonance and magnetic dipole quasi-bound state in the continuum in an all-dielectric hollow metasurface, Laser Phys. 32 (2022) 025403.
[31] J. Xing, H. Li, S. Yu, Y. Shi, T. Zhao, Multiple Fano resonances driven by bound states in the continuum in an all-dielectric nanoarrays system, AIP Adv. 13 (2023) 035212.
[32] H. Chen, X. Fan, W. Fang, S. Cao, Q. Sun, Investigation of multiple high quality-factor Fano resonances in asymmetric nanopillar arrays for optical sensing, Photonics 11 (2024) 68.
[33] J. Wang, W. Liu, Z. Wei, H. Meng, Hn Liu, J. Guo, M. Yang, Y. Song, L. Xiang, Z. Huang, et al., A bifunctional silicon dielectric metasurface based on quasi-bound states in the continuum, Nanomaterials 11 (9) (2021) 2357.
[34] Y. Cai, Y. Huang, K. Zhu, H. Wu, Symmetric metasurface with dual band polarization-independent high-Q resonances governed by symmetry-protected BIC, Opt Lett. 46 (2021) 4049–4052.
[35] H. Fan, J. Li, C. Liu, Y. Sun, Y. Wang, X. Wang, T. Wu, H. Ye, Y. Liu, Polarization-independent tetramer metasurface with multi-Fano resonances based on symmetry-protected bound states in the continuum, Opt Commun. 525 (2022) 128864.
[36] Z. Liao, Q. Ma, L. Wang, Z. Yang, M. Li, F. Deng, W. Hong, Guiding-mode-assisted double-BICs in an all-dielectric metasurface, Opt Express 30 (2022) 24676–24688.
[37] C. Zhou, S. Li, Y. Wang, M. Zhan, Multiple toroidal dipole Fano resonances of asymmetric dielectric nanohole arrays, Phys. Rev. B 100 (2019) 195306.
[38] P. Wu, C. Liao, V. Savinov, Optical anapole metamaterial, ACS Nano 12 (2018) 1920–1927.
[39] L. Xu, K.Z. Kamali, L. Huang, M. Rahmani, A. Smirnov, Dynamic nonlinear image tuning through magnetic dipole quasi-BIC ultrathin resonators, Adv. Sci. 6 (2019) 1802119.
[40] P. Bing, J. Sui, G. Wu, X. Guo, Z. Li, L. Tan, J. Yao, Analysis of dual-channel simultaneous detection of photonic crystal fiber sensors, Plasmonics 15 (2020) 1071–1076.
[41] M.F. Limonov, Fano Resonance for Applications Advances in Optics and Photonics, vol. 13, 2021, pp. 703–771.
[42] A. Miroshnichenko, S. Flach, Y. Kivshar, Fano resonances, nanoscale structures 82 (3) (2010) 2257–2298.
[43] J. Lv, Y. Ren, D. Wang, et al., Optical switching with high-Q Fano resonance of all-dielectric metasurface governed by bound states in the continuum, Opt Express 32 (16) (2024) 28334–28347.
[44] D. Zhang, Y. Wang, Y. Zhu, et al., Ultra-high Q resonances governed by quasi-bound states in the continuum in all-dielectric THz metamaterials, Opt Commun. 520 (2022) 128555.
[45] Y. Wang, Z. Han, Y. Du, J. Qin, Ultrasensitive terahertz sensing with high-Q toroidal dipole resonance governed by bound states in the continuum in all-dielectric metasurface, Nanophotonics 10 (4) (2021) 1295–1307.
[46] A. Alexopoulos, Effective-medium theory of surfaces and metasurfaces containing two-dimensional binary inclusions, Phys. Rev. E: Stat., Nonlinear, Soft Matter Phys. 81 (4) (2010) 046607.
[47] L. Guo, Z. Zhang, Q. Xie, W. Li, F. Xia, M. Wang, H. Feng, C. You, M. Yun, Toroidal dipole bound states in the continuum in all-dielectric metasurface for high-performance refractive index and temperature sensing, Appl. Surf. Sci. 615 (2023) 156408.
[48] J. Lv, W. Li, J. Wang, et al., High-sensitivity strain sensor based on an asymmetric tapered air microbubble Fabry-Pérot interferometer with an ultrathin wall, Opt Express 32 (11) (2024) 19057–19068.
[49] T. Liu, Y. Huo, Z. Liao, C. Zhao, T. Zhang, C. Xu, Z. Zhang, High Q-factor multiple Fano resonances in all-dielectric metasurface based on quasi-bound states in the continuum, Opt. Rev. 31 (2024) 194–202.